PAPER • OPEN ACCESS

Generation of interferometrically stable pulse pairs from a free-electron laser using a birefringent interferometer

To cite this article: B Ardini *et al* 2024 *J. Phys. B: At. Mol. Opt. Phys.* **57** 075402

View the article online for updates and enhancements.

Generation of interferometrically stable pulse pairs from a free-electron laser using a birefringent interferometer

B Ardini[1,5] [ID], **F Richter**[2,5] [ID], **L Uboldi**[1] [ID], **P Cinquegrana**[3], **M Danailov**[3], **A Demidovich**[3] [ID], **S D Ganeshamandiram**[2] [ID], **S Hartweg**[2] [ID], **G Kurdi**[3], **F Landmesser**[2] [ID], **M Michelbach**[2] [ID], **A Ngai**[2] [ID], **I Nikolov**[3], **N Rendler**[2], **F Stienkemeier**[2] [ID], **D Uhl**[2] [ID], **L Bruder**[2] [ID], **G Cerullo**[1] [ID] and **C Manzoni**[4,*] [ID]

[1] Department of Physics, Politecnico Milano, Piazza Leonardo da Vinci 32, 20133 Milano, Italy
[2] Institute of Physics, University of Freiburg, Hermann-Herder-Str. 3, 79104 Freiburg, Germany
[3] Elettra-Sincrotrone Trieste S.C.p.A., 34149 Basovizza (Trieste), Italy
[4] Institute for Photonics and Nanotechnology, CNR, Piazza Leonardo da Vinci 32, 20133 Milano, Italy

E-mail: cristian.manzoni@polimi.it

CrossMark

Abstract

We present a compact, intrinsically stable common path interferometer for the seeding of free-electron lasers (FELs). The interferometer can handle the required ultraviolet seed wavelengths and features an excellent phase stability of 10 mrad at 265 nm. By seeding the FEL FERMI, we demonstrate the generation of extreme ultraviolet (XUV) pulse pairs with tunable delay and a delay stability of 6 as at 52.5 nm. Prospective applications are Fourier transform spectroscopy, nonlinear spectroscopy and coherent control experiments in the XUV and x-ray domain.

Keywords: interferometers, FEL, birefringence

1. Introduction

The development of high brilliance XUV and x-ray FELs with femto- to attosecond pulse durations opens up many possibilities for nonlinear spectroscopy [1] and coherent control experiments [2]. Many of the proposed experimental schemes [3–5] require the generation of sequences of multiple XUV/x-ray pulses with precisely controlled timing. However, already the generation of two pulse replicas and their precise timing control is very challenging to achieve in the XUV/x-ray domain. In particular, for interferometric applications, sub-cycle phase/delay stability is required, which becomes

increasingly demanding at short wavelengths. This explains why, to date, only a few interferometric time-domain experiments have been reported in the XUV to X-ray regime [2, 6–13] or suggested theoretically [14, 15].

At much longer wavelengths, in the visible to infrared domain, the generation of pulse replicas with interferometric timing stability is well established [16–18]. Translating these concepts directly to the XUV/x-ray domain is difficult due to the lack of suitable optics, as well as the high demand on mechanic stability posed by the much shorter wavelengths. An alternative strategy is the preparation of the pulse sequence at a longer wavelength, followed by the transfer to the XUV/x-ray domain with a nonlinear conversion process, such as the high-gain harmonic generation (HGHG) in a seeded FEL [19]. The feasibility of this concept has been demonstrated for the generation of phase-locked [20] and phase-modulated (PM) pulse pairs [7, 21]. So far, in [20] the accessible delay range was strongly limited. Using the PM approach, interferometric spectroscopy has been demonstrated with high sensitivity [7, 8, 22]. Yet, the pulse delay is actually not precisely controlled

J. Phys. B: At. Mol. Opt. Phys. **57** (2024) 075402

B Ardini *et al*

in this scheme; instead, the delay jitter is corrected in a post processing step [22]. In addition, when changing the delay, a small transverse spatial offset between the replicas is introduced, which leads to loss of interferometric contrast. These limitations prevent coherent control applications where active manipulation of the phase/delay is needed [23].

Hence, an interferometer setup suitable for seeding an XUV FEL featuring sufficient delay range and direct sub-cycle delay control would enable a large number of nonlinear spectroscopy applications. A suitable interferometer for seeding an FEL must fulfil the following demands: (i) <10 as timing jitter, (ii) compatibility with UV wavelengths (260–360 nm) and ≈2 GW pulse peak power, (iii) low beam pointing instabilities, due to tens of meters of beampath of the seed pulses after the interferometer.

Typically, time-delayed pulse replicas in the UV/visible are generated by amplitude division interferometers such as a Michelson or a Mach–Zehnder. Interferometric stability requires a delay precision much better than the optical period, so that any mechanical vibration of one arm of the interferometer with amplitude of a fraction of the wavelength (tens of nanometers in the visible) would spoil the interference pattern. This calls for active stabilization of the interferometer [17] or tracking the mirrors position with an auxiliary beam [24]. Alternatively, phase-locked pulse pairs can be produced using pulse shapers, which intrinsically provide interferometric stability due to the common path of the two pulses. 4f zero-dispersion pulse shapers, with a liquid crystal spatial light modulator or an acousto-optic modulator [25] placed in the Fourier plane, or an inline acousto-optic programmable dispersive filter [26], can be used. However, pulse shapers considerably increase the complexity and cost of the experimental setup.

Common-path birefringent interferometers overcome these limitations and achieve high passive delay stability of the generated replicas. Instead of separating the two replicas in space, as in a Michelson interferometer, a birefringent interferometer projects them onto two perpendicular polarization states, which are delayed with very high accuracy by varying the thickness of a birefringent material and then projected back to a common polarization state, to allow their interference on the detector. Following this approach, some of the authors introduced a birefringent interferometer, the Translating-Wedge-based Identical pulses eNcoding System (TWINS) [27], as a simple and compact optical device which generates two delayed, phase-locked collinear replicas of an input pulse. TWINS has shown considerable experimental versatility and, while originally conceived for two-dimensional electronic spectroscopy [28], it has been further developed and applied to hyperspectral imaging [29], excitation emission spectroscopy, Raman microscopy [30] and even in the combination with high-harmonic generation (HHG) [6]. A schematic of the TWINS interferometer is shown in figure 1.

In this paper we report on the application of the TWINS interferometer to the generation of phase-locked XUV pulse pairs from the FERMI FEL facility. By placing the TWINS in the path of the 261 nm seed beam, we generate a pair of UV seed pulses with exceptionally low delay fluctuations (1.43 as,

corresponding to a phase stability of 10 mrad). Thanks to the HGHG process, this stability is transferred to the XFEL pulses, resulting in delay fluctuations of 6 as at the fifth harmonic, which corresponds to 1/30 of the optical cycle. Such performances, in combination with the simplicity of the experimental setup, make this configuration very promising for applications to nonlinear spectroscopy and coherent control in the XUV.

2. Materials and methods

2.1. The birefringent interferometer

The TWINS interferometer is based on birefringent materials, which are characterized by a privileged direction named optical axis. When a light waveform propagates in such material, ordinary polarization (i.e. normal to the optical axis) and extraordinary polarization (i.e. parallel to the optical axis) experience two different refractive indices (n_o and n_e respectively) and hence travel with different velocities, thus accumulating a relative delay proportional to the propagation length. By varying the material thickness, an arbitrary delay can be imposed on the two polarization components. Since both replicas follow the same optical path, they do not accumulate relative path-length fluctuations, as in a standard Michelson interferometer, so that their delay is fixed with unprecedented stability.

Figure 1 sketches the structure of the TWINS interferometer used in our experiments, equivalent to the systems used in references [6, 29, 30]. It consists of two birefringent blocks A and B sandwiched between the polarizers P1 and P2. The optical axes of the two blocks are mutually crossed, so that they introduce delays with opposite signs. Block B is a parallel-faces plate with fixed thickness, which introduces a constant delay, while block A is cut into two wedges with an overall variable thickness which depends on the relative position of the wedges, hence introducing a variable delay with the opposite sign with respect to block B. As a result, the interferometer introduces an arbitrary delay which can be finely adjusted by moving one of the wedges. With respect to the original TWINS scheme [27], the current version does not keep the arrival time of one of the two replicas fixed in an absolute frame of reference.

In the current experiment, the birefringent material is α-barium borate (α-BBO); block A has apex angle 7° and a transverse size of 25 mm, and block B has thickness of 3.7 mm. With these design parameters, the maximum delay range of our TWINS is 1.1 ps. The clear aperture of the interferometer is 2×2 cm^2, which is sufficient to accommodate a high energy ultrashort pulse without introducing nonlinear phase distortions. Polarizer P1 is at 45° with respect to the birefringent optical axes and projects the input field polarization so that its energy is equally distributed between the ordinary and extraordinary directions; it can be omitted if the input beam has already the correct polarization. Polarizer P2, on the other hand, projects the two orthogonally polarized replicas on the same polarization, thus allowing them to interfere. The working spectral range of the interferometer is determined by the transparency of the polarizer and the birefringent blocks
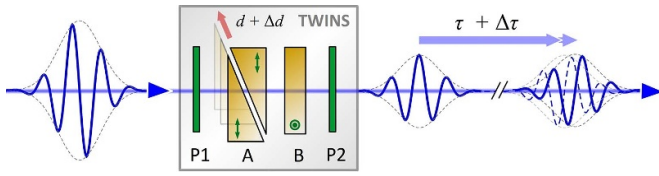
Figure 1. The TWINS setup. A: birefringent wedges with optical axis in the plane of the figure (green double lines); B: birefringent plate with optical axis perpendicular to the plane of the figure (green circle); P1, P2: polarizers at 45° with respect to the birefringent optical axes.

(for α-BBO it ranges from 200 nm to 3.5 μm wavelength). The system works with any pulse duration (a suitable compression system is required to compensate for the dispersion added by propagation in the blocks). The pulse peak intensity must be kept below the damage threshold of the birefringent crystal and below the onset of unwanted third-order nonlinear optical effects: typically, the interferometer can work with pulses with peak intensities below 1 GW cm^{-2}. The translation of the movable wedge is controlled by a piezoelectric motor (Physik Instrumente Q-521.330, minimum incremental motion 50 nm). In the following, the wedge position will be expressed as $d + \Delta d$, where d is the position of the motor corresponding to the group delay τ between the pulses, while Δd is the additional motor translation required to introduce the phase delay $\Delta \tau$; $d = 0$ corresponds to $\tau = 0$.

2.2. Characterization in the UV spectral range

To characterize the static and dynamic capabilities of the interferometer, we performed spectral interferometry in the UV range. In spectral interferometry, the field $E(t)$ of a pulse with spectrum $S(f)$ centered at frequency f_0 interferes with its delayed replica $aE(t - T)$, where T is the delay and a is a scaling factor. The resulting spectrum is:

$$S_{TOT}(f) = S(f) \left[\left(1 + a^2\right) + 2a \cos\left(2\pi f T\right) \right]. \quad (1)$$

It is proportional to the spectrum of each individual field, modulated by a cosine function which gives rise to spectral interference fringes. In the framework of our experiment, T can be written as $T = \tau + \Delta \tau$; here τ is the group delay between the pulse replicas and is larger than the transform-limited duration of the pulse, while $\Delta \tau \ll \tau$ is a delay shift of the order of a few optical cycles, and corresponds to a phase delay. In this case, the cosine can be approximated as:

$$\cos\left(2\pi f T\right) \approx \cos\left(2\pi f \tau + 2\pi f_0 \Delta \tau\right) = \cos\left(2\pi f \tau + \varphi\right). \quad (2)$$

Equations (1) and (2) show that from spectral interferometry measurements we can obtain three pieces of information: from the period Δf of the spectral modulation we get the group delay $\tau = 1/\Delta f$; the shift φ of the spectral fringes enables the retrieval of the phase delay $\Delta \tau$; finally, the modulation depth (also called interferometric contrast) conveys a, and is maximum when $a = 1$, i.e. when the two fields are perfectly balanced. Therefore spectral interferometry enabled us to perform the calibration of the interferometer, which is an intrinsic
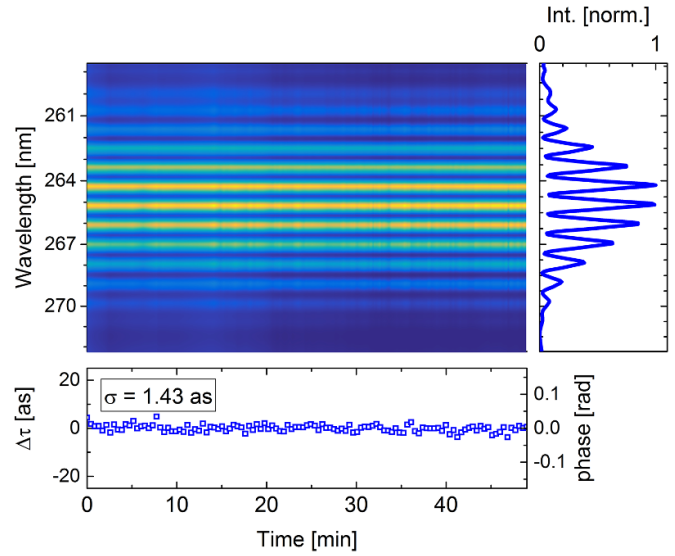
Figure 2. Characterization of the static stability of the interferometer. Main panel: sequence of interferograms, obtained at constant pulse delay $\tau = 255$ fs. Right panel: individual spectrum. Lower panel: retrieved phase-delay fluctuation.

property that holds independently from the light source and the application. The characterization was performed with a system based on an amplified Ti:sapphire laser. UV light was obtained by frequency doubling the output of a broadband optical parametric amplifier in the visible [31], thus generating broadband UV pulses in the range from 260 nm to 270 nm. The polarization of the pulses was set at 45° with respect to the optical axes of the birefringent blocks; the cross-polarized pulse pair generated by the interferometer was projected to the same polarization by means of a wire-grid polarizer (Moxtek ProFlux Nanowire UVT240A) and sent to a high-resolution spectrometer, synchronized to the 1 kHz laser repetition rate.

The static stability of the interferometer was characterized by fixing the wedge position d (2.6 mm) to keep the two replicas at a constant delay τ (255 fs) and measuring the spectrum, which is modulated due to spectral interference. A sequence of output spectra was then measured for 50 min; each recorded spectrum is the average of 400 consecutive shots [32]. The result is shown in figure 2. The right panel shows a UV spectrum: its deep modulation reveals the high interferometric contrast (85%) provided by the birefringent interferometer. The main panel represents the sequence of spectra, from which one can extract the phase delay, which is proportional to the phase shift of the interference fringes, as well as the group delay, which is inversely proportional to the spectral modulation period.

By analysing the phase of the spectral modulation, we retrieved the phase delay reported in the lower panel. We provide both the phase fluctuation $\Delta \phi$ and the temporal fluctuation $\Delta \tau = \Delta \phi \lambda / (2\pi c)$ of the spectral component at $\lambda = 265$ nm. The standard deviation of the phase delay is $\sigma_{\Delta \tau} = 1.43$ as, corresponding to $\sigma_{\Delta \phi} = 10.15$ mrad. Such fluctuation is better than 1/600 of the optical cycle at 265 nm wavelength, and reveals the excellent static stability of the interferometer.

The dynamic behaviour of the interferometer was characterized by repeating the same measurement while
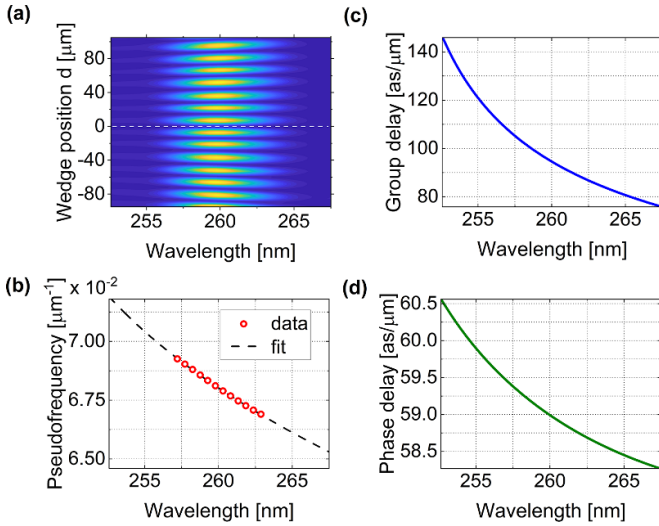
Figure 3. (a) Interferogram as function of the motor position. The dashed white line indicates the zero delay position. (b) Spectral calibration of TWINS (red circles) at the spectrometer optical wavelength and quadratic fit (dashed line). (c) Group delay calculated from the calibration fit shown in panel (b). (d) Phase delay calculated from the calibration fit shown in panel (b).

scanning the wedge position by $\Delta d = \pm 3.5\,\mu\text{m}$ around d. During the scan, the motor position was controlled by a feedback loop which checks that the motor position (provided by an internal encoder) is on target. From the shift of the spectral fringes of the recorded interferograms we retrieved the differential delay $\Delta\tau$. The results are reported in section 3.1, lower panel of figure 6 (green circles), where we discuss the same measurements performed in the XUV range. A fit of $\Delta\tau$ with a linear function yields a slope of (60.70 ± 0.06) as μm^{-1}. The standard deviation of the residual between the experimental delay and the fitting line is 1.29 as, comparable to the static stability.

Using the same source and spectrometer, we performed also the so-called spectral calibration of the interferometer: this is obtained by acquiring a sequence of interferograms as a function of the motor position around $d = 0$. This calibration not only enables using the interferometer as spectrometer, but also allows to draw a first estimation of the phase and group delay per unit motor displacement. The results are shown in figure 3. Panel (a) is the 2D map with the sequence of spectra for different values of Δd. In practice, the map is a spectrally resolved linear autocorrelation of the pulse with the symmetry axis around $\tau = 0$. By taking the Fourier transform with respect to d of each horizontal cut of the map (corresponding to a given optical frequency f), one obtains the spectral calibration of the interferometer, provided in panel (b). The curve associates f to the pseudofrequency f_p (i.e. the reciprocal of the motor position).

From the spectral calibration, we estimated the phase and the group delay introduced by the interferometer per unit motor displacement; the results are shown in panels (c) and (d) respectively. Note that while in a Michelson or a Mach–Zehnder interferometer, group and phase delays have the same values and do not depend on f, in our interferometer

they are different and are wavelength-dependent because the delay arises from propagation in a dispersive bulk material. At 261 nm, the estimated phase delay is 59 as μm^{-1} (in very close agreement with the slope obtained from the dynamic characterization), while the group delay is 91.2 as μm^{-1}.

3. Results and discussion

3.1. Interferometric stability in the XUV spectral domain

To enable interferometric spectroscopy in the XUV spectral domain, the TWINS interferometer was placed in the beam path of the seed laser at the FEL facility FERMI. Figure 4 shows the experimental setup, which is similar to the one described in [20]. Briefly, a Ti:Sa oscillator is frequency tripled with a set of nonlinear crystals to yield pulses at 261 nm, of 50 Hz repetition rate. The pulses are pre-compressed with a grating compressor consisting of a single pass through two transmission gratings. The pulses are subsequently sent to the TWINS interferometer to yield two delayed and phase-locked seed pulses, and then to the modulator section of the FEL, where the replicas overlap with a relativistic electron beam. We note that the total propagation length of the seed pulses from the TWINS to the modulator is ≈ 30 m; this calls for a perfect collinearity of the pulse replicas and high beam pointing stability to observe high-contrast interference during a delay scan. The electro-magnetic field of the intense seed laser pulses imprints an energy modulation to the electron bunch. A dispersive magnet (inside the dispersive section of the FEL) converts this modulation to a density modulation, resulting in micro-bunching of the electron density. Passing these micro-bunched electron packages through the subsequent undulators (radiators) leads to coherent emission at a specific harmonic of the seed laser (the fifth in this experiment), set by the undulator gap (more details in [19]). Upon this process, the properties of the seed pulses are transferred to the generated XUV pulses, enabling the generation of XUV pulse pairs with controllable delay. The spectral interference fringes of the generated XUV pulse pairs are recorded single-shot with an XUV spectrometer.

The 261 nm-seed pulses after the TWINS were characterized in the time domain by self-diffraction third-order autocorrelation measurements. We collected autocorrelation traces for four different TWINS wedge positions d at steps of 0.5 mm, and the results are reported in figure 5(a). As the TWINS splits the seed pulse into two replicas, three peaks are visible in the autocorrelation intensity plot; in particular, the lateral peaks are the cross-correlation terms of the two replicas, and their distance from the main peak conveys the pulses delay τ. By fitting the lateral peaks with a Gaussian function (see inset of panel (a)) we could retrieve the position of their centroids, as well as the correlation width. From the centroids delay as a function of the motor position, we obtained that the group delay introduced by the TWINS (see panel (b)) is (97.03 ± 0.17) as μm^{-1} (or equivalently (97.03 ± 0.17) fs mm^{-1}), in very good agreement with the independent interferometric calibration reported in section 2.2, figure 3 at 261 nm wavelength. The FWHM of each Gaussian fit is

J. Phys. B: At. Mol. Opt. Phys. **57** (2024) 075402

B Ardini *et al*
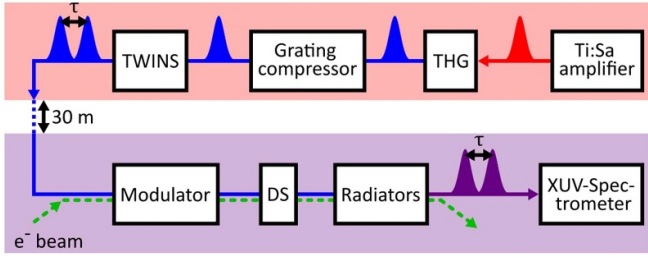
Figure 4. Block diagram of the experimental setup at the FEL FERMI. Red area: seed laser setup, purple area: FEL scheme, THG: third harmonic generation, DS: dispersive section.
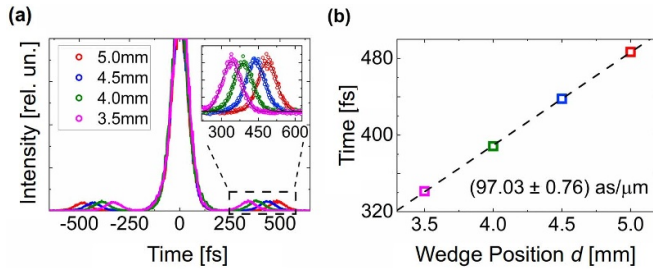

Figure 5. (a) Autocorrelation intensities obtained for the wedge absolute positions d indicated in the legend. Inset: detail of the cross-correlation peaks inside the dashed-line box. The corresponding Gaussian fit lines are superimposed to the data points. (b) Centroid position of each Gaussian fit as a function of d. Their linear trend is represented by the dashed fitting line; its slope is also given.

(91.70 ± 0.83) fs, corresponding to a pulse duration of ≈ 74.7 fs, very close to the transform limit.

In the following we will show that the seeding mechanism of the FEL FERMI allows for the generation of two XUV pulses by the HGHG process, in which the delay between the pulses can be controlled with interferometric precision. For the FEL seeding, since the interaction axis of the FEL modulator acts as a polarizer, P2 at the TWINS output was removed and replaced by a half-waveplate to rotate both pulses by $45°$.

To characterize the XUV pulse delay, we performed also in this case spectral interferometry: we carried out a scan with Δd ranging from $= -3.5 \, \mu$m to $3.5 \, \mu$m around $d \approx 2.06$ mm corresponding to a delay range from -210 as to 210 as around $\tau = 200$ fs. This is equivalent to ≈ 0.46 optical cycles at 261 nm and ≈ 2.3 optical cycles at 52.5 nm. The delay offset of $\tau = 200$ fs was chosen sufficiently large to avoid nonlinear mixing of the seed pulses in the HGHG process. For each motor position, we acquired the fringe pattern of the two overlapping XUV pulses with an XUV spectrometer on a single shot basis, at the 50 Hz repetition rate of the FEL [32]. The result is reported in figure 6; the main panel shows a sequence of the resulting interferograms as a function of the wedge position. Each interferogram is the average of 100 spectra per recorded position. In order to account for the FEL fluctuation, each spectrum was normalized by dividing to the pulse energy (estimated as the weight of the first score after performing the Principal Component Analysis on the entire trace).
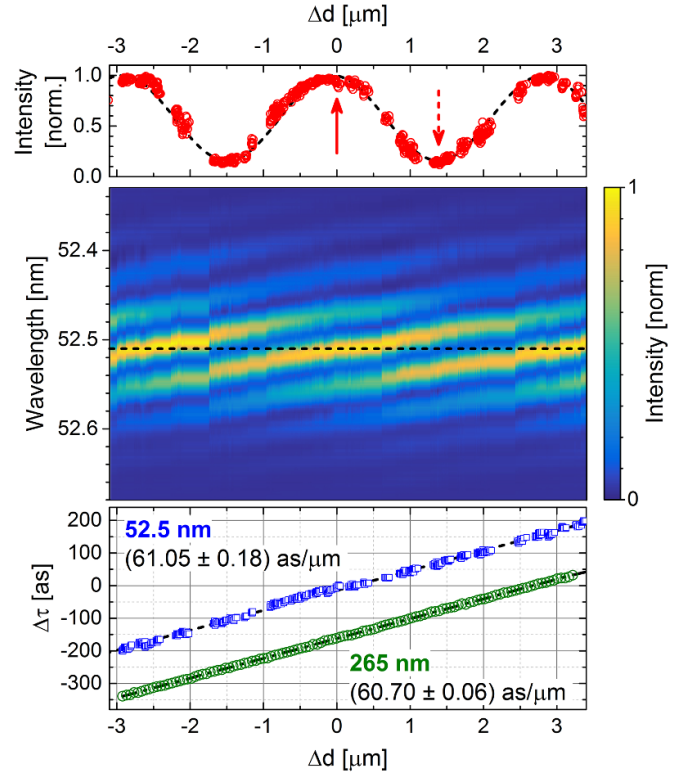
Figure 6. Sequence of the interferograms of XUV light as a function of the interferometer wedge position, provided by the inner encoder of the motor. The motor moves around position $d = 2.06$ mm. For representation purposes only, the gaps in the 2D map, originated from a non uniform stepping of the motor (see text), were filled with the same spectra as before the gaps. Upper panel: a cut of the map at 52.51 nm (dashed line of main panel). Lower panel: Phase delay $\Delta\tau$ retrieved from the experimental interferograms, as a function of motor position. Blue dots: XUV pulses at 52.5 nm; Green dots: UV pulses at 265 nm. The dataset of the UV pulses has been vertically displaced for clarity. The dashed lines are fitting each series; their slope is also given.

The top panel of figure 6 shows the horizontal cut of the sequence of interferograms at 52.51 nm, indicated by the dashed line. The cut dataset, in accordance with equation (1), has been fitted with a cosine function with retrieved period of 2.87 μm and a contrast of 72.7%. The observable discontinuity within the sequence of spectra are due to a non uniform stepping of the motor, originating from the fact that in this specific experiment the motor position was commanded in open-loop, i.e. its position was not monitored and hence any error was not retroactively corrected. The feedback was not implemented in the experimental control software of the end station of FERMI during the beamtime, but in general the software could be upgraded to closed-loop operation. However, despite the measurement was performed in open-loop, the XUV interferograms show very high quality and the delay scan follows the sinusoidal phase modulation with high precision.

From the shift of the spectral fringes of the recorded interferograms we retrieved the differential delay $\Delta\tau$. The results are shown in the lower panel of figure 6 (blue squares), together with the phase delay obtained with the similar measurement performed at 265 nm (green circles) mentioned in

J. Phys. B: At. Mol. Opt. Phys. **57** (2024) 075402

B Ardini *et al*
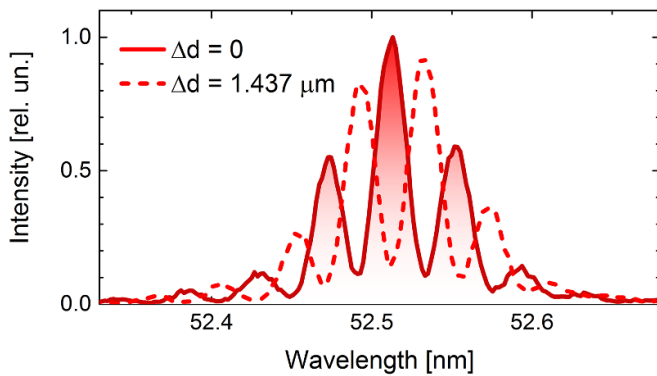
Figure 7. Two interferograms at positions 0 and 1.437 μm, respectively indicated by the solid and dashed red lines in figure 6, upper panel.

section 2.2. The data have been fitted with a linear function and yield a slope of (61.05 ± 0.18) as μm^{-1} in very good agreement with the slope at 265 nm, confirming that the phase-delay of the FEL pulses matches the delay of the seed UV pulses. The residuals between the experimental delay and the fitting line have standard deviation of 6 as. The larger residual of the XUV delay with respect to the seed pulse may be attributed to instabilities introduced in the HGHG process as well as to timing jitter between the seed laser and the electron bunch [7].

An important feature of the demonstrated setup is the ability for active phase control between two XUV pulse replicas. As an example, figure 7 shows two XUV interferograms acquired at positions 0 and 1.437 μm respectively, corresponding to exactly a π phase shift (see solid and dashed arrows in upper panel of figure 6). The precise, deterministic phase control in combination with the high interference contrast provide the requirements for monochromatic XUV coherent control experiments, similar to previously demonstrated bichromatic schemes [2, 33]. An interesting application of monochromatic XUV coherent control has been recently reported for a tabletop HHG source studying quantum mechanical entanglement in photoionization [34]. Another possible application is the mode-selective excitation in the investigation of ultrafast molecular dynamics. For instance, the sensitivity of interatomic coulombic decay on the vibrational mode in the HeNe dimer has been shown [35]. First interferometric experiments of this system were demonstrated, implying the feasibility of such experiments [8]. Other parameters important in view of spectroscopic and coherent control applications, are the available delay range and the scalability to higher photon energy. In the presented scheme, temporally overlapping seed pulses lead to nonlinear mixing in the HGHG process [21]. This limits the available minimum delay to roughly twice the seed pulse duration. The maximum achievable range is given by the length of the electron bunch that is seeded, which poses a limit of roughly 1 ps [8]. We note that the seed interferometer supports a larger tuning range and, hence, does not limit the available delay range. This is in contrast to a similar scheme, based on birefringent optics, previously reported [20],

which was limited to small delay ranges. The interferometric control at higher photon energies is limited by the phase jitter of the setup, posing a limit for the attainable maximum photon energy. The phase jitter is determined by a combination of the stability of the seed-laser interferometer and the fluctuations introduced in the HGHG process. The scaling of the latter factor with harmonic order needs to be investigated in the future to determine an upper limit for the photon energy at which interferometric applications are still feasible. However, our study shows that it is possible to apply the technique for photon energies up to at least 25 eV.

4. Conclusions

The generation of interferometrically stable XUV pulse pairs with controllable delay is required for a number of nonlinear spectroscopy applications, including two-dimensional spectroscopy and coherent control. Direct manipulation of the XUV pulses is technically challenging, due to the very short wavelengths and the consequent extreme requirements on the mechanical stability of the interferometer. The FERMI FEL, which works with seeding in combination with the HGHG process, allows one to manipulate the UV seed pulses using established methodologies. In addition, FELs provide the required high intensities for nonlinear spectroscopy and quantum control experiments. Here we report on the use of a birefringent interferometer, the TWINS, to generate UV pulse pairs with phase delay fluctuation of only 1.43 as (corresponding to a phase jitter of 10 mrad). These properties are then transferred to the XUV pulses generated via HGHG which, despite the nonlinearities of the FEL process, maintain a remarkably high delay stability of 6 as (215 mrad). Due to the compactness, simplicity and low cost of the TWINS interferometer, we envision that this approach could be adopted in all seeded FELs and enable a variety of nonlinear optical spectroscopy experiments in a so far unexplored wavelength range.

Data availability statement

The data that support the findings of this study are openly available at the following URL/DOI: 10.5281/zenodo. 10059067.

Acknowledgment

J. Phys. B: At. Mol. Opt. Phys. **57** (2024) 075402

B Ardini *et al*

Conflict of interest

The authors declare no conflicts of interest.

ORCID iDs

B Ardini ⬤ https://orcid.org/0000-0003-2188-5867
F Richter ⬤ https://orcid.org/0000-0002-5274-5851
L Uboldi ⬤ https://orcid.org/0000-0002-6969-4894
A Demidovich ⬤ https://orcid.org/0000-0003-2355-2257
S D Ganeshamandiram ⬤ https://orcid.org/0000-0002-4278-1584
S Hartweg ⬤ https://orcid.org/0000-0002-3053-683X
G Kurdi ⬤ https://orcid.org/0000-0001-8600-3509
F Landmesser ⬤ https://orcid.org/0000-0001-6748-8862
M Michelbach ⬤ https://orcid.org/0000-0002-8157-1504
A Ngai ⬤ https://orcid.org/0000-0002-1098-9794
F Stienkemeier ⬤ https://orcid.org/0000-0001-6014-8013
D Uhl ⬤ https://orcid.org/0000-0002-5988-001X
L Bruder ⬤ https://orcid.org/0000-0001-9992-9925
G Cerullo ⬤ https://orcid.org/0000-0002-9534-2702
C Manzoni ⬤ https://orcid.org/0000-0002-4169-8869

References

[1] Chergui M, Beye M, Mukamel S, Svetina C and Masciovecchio C 2023 Progress and prospects in nonlinear extreme-ultraviolet and x-ray optics and spectroscopy *Nat. Rev. Phys.* **5** 578–96

[2] Prince K C *et al* 2016 Coherent control with a short-wavelength free-electron laser *Nat. Photon.* **10** 176–9

[3] Mukamel S, Healion D, Zhang Y and Biggs J D 2013 Multidimensional attosecond resonant x-ray spectroscopy of molecules: lessons from the optical regime *Annu. Rev. Phys. Chem.* **64** 101–27

[4] Kowalewski M, Bennett K, Dorfman K E and Mukamel S 2015 Catching conical intersections in the act: monitoring transient electronic coherences by attosecond stimulated x-ray Raman signals *Phys. Rev. Lett.* **115** 193003

[5] Palacios A, González-Castrillo A and Martín F 2014 Molecular interferometer to decode attosecond electron–nuclear dynamics *Proc. Natl Acad. Sci.* **111** 3973–8

[6] Jansen G S M, Rudolf D, Freisem L, Eikema K S E and Witte S 2016 Spatially resolved Fourier transform spectroscopy in the extreme ultraviolet *Optica* **3** 1122

[7] Wituschek A *et al* 2020 Tracking attosecond electronic coherences using phase-manipulated extreme ultraviolet pulses *Nat. Commun.* **11** 883

[8] Uhl D *et al* 2022 Extreme ultraviolet wave packet interferometry of the autoionizing HeNe dimer *J. Phys. Chem. Lett.* **13** 8470–6

[9] Usenko S, Przystawik A, Alexander Jakob M, Lamberto Lazzarino L, Brenner G, Toleikis S, Haunhorst C, Kip D and Laarmann T 2017 Attosecond interferometry with self-amplified spontaneous emission of a free-electron laser *Nat. Commun.* **8** 15626

[10] Usenko S *et al* 2020 Auger electron wave packet interferometry on extreme timescales with coherent soft x-rays *J. Phys. B: At. Mol. Opt. Phys.* **53** 244008

[11] Skruszewicz S *et al* 2021 Table-top interferometry on extreme time and wavelength scales *Opt. Express* **29** 40333–44

[12] Bellini M, Lyngå C, Tozzi A, Gaarde M B, Hänsch T W, L'Huillier A and Wahlström C-G 1998 Temporal coherence of ultrashort high-order harmonic pulses *Phys. Rev. Lett.* **81** 297–300

[13] Cavalieri S, Eramo R, Materazzi M, Corsi C and Bellini M 2002 Ramsey-type spectroscopy with high-order harmonics *Phys. Rev. Lett.* **89** 133002

[14] Giannessi L *et al* 2018 Coherent control schemes for the photoionization of neon and helium in the extreme ultraviolet spectral region *Sci. Rep.* **8** 7774

[15] Khokhlova M A, Cooper B, Ueda K, Prince K C, Kolorenč P, Ivanov M Y and Averbukh V 2019 Molecular Auger interferometry *Phys. Rev. Lett.* **122** 233001

[16] Warren W S, Rabitz H and Dahleh M 1993 Coherent control of quantum dynamics: the dream is alive *Science* **259** 1581–9

[17] Wehner M U, Ulm M H and Wegener M 1997 Scanning interferometer stabilized by use of Pancharatnam's phase *Opt. Lett.* **22** 1455

[18] Kolesnichenko P V, Wittenbecher L and Zigmantas D 2020 Fully symmetric dispersionless stable transmission-grating Michelson interferometer *Opt. Express* **28** 37752

[19] Allaria E *et al* 2012 Highly coherent and stable pulses from the FERMI seeded free-electron laser in the extreme ultraviolet *Nat. Photon.* **6** 699–704

[20] Gauthier D, Rebernik Ribič P, De Ninno G, Allaria E, Cinquegrana P, Bojanov Danailov M, Demidovich A, Ferrari E and Giannessi L 2016 Generation of phase-locked pulses from a seeded free-electron laser *Phys. Rev. Lett.* **116** 024801

[21] Wituschek A *et al* 2020 High-gain harmonic generation with temporally overlapping seed pulses and application to ultrafast spectroscopy *Opt. Express* **28** 29976–90

[22] Uhl D *et al* 2022 Improved stabilization scheme for extreme ultraviolet quantum interference experiments *J. Phys. B: At. Mol. Opt. Phys.* **55** 074002

[23] Brumer P W and Shapiro M 2003 *Principles of the Quantum Control of Molecular Processes* 1 edn (Wiley)

[24] Helbing J and Hamm P 2011 Compact implementation of Fourier transform two-dimensional IR spectroscopy without phase ambiguity *J. Opt. Soc. Am.* B **28** 171–8

[25] Kearns N M, Jones A C, Bohlmann Kunz M, Allen R T, Flach J T and Zanni M T 2019 Two-dimensional white-light spectroscopy using supercontinuum from an all-normal dispersion photonic crystal fiber pumped by a 70 MHz Yb fiber oscillator *J. Phys. Chem.* A **123** 3046–55

[26] Verluise F, Laude V, Cheng Z, Spielmann C and Tournois P 2000 Amplitude and phase control of ultrashort pulses by use of an acousto-optic programmable dispersive filter: pulse compression and shaping *Opt. Lett.* **25** 575–7

[27] Brida D, Manzoni C and Cerullo G 2012 Phase-locked pulses for two-dimensional spectroscopy by a birefringent delay line *Opt. Lett.* **37** 3027–9

[28] Réhault J, Maiuri M, Oriana A and Cerullo G 2014 Two-dimensional electronic spectroscopy with birefringent wedges *Rev. Sci. Instrum.* **85** 123107

[29] Perri A, Nogueira de Faria B E, Teles Ferreira D C, Comelli D, Valentini G, Preda F, Polli D, de Paula A M, Cerullo G and Manzoni C 2019 Hyperspectral imaging with a TWINS birefringent interferometer *Opt. Express* **27** 15956–67

[30] Ardini B *et al* 2023 High-throughput multimodal wide-field Fourier-transform Raman microscope *Optica* **10** 663–70

J. Phys. B: At. Mol. Opt. Phys. **57** (2024) 075402

B Ardini *et al*

[31] Borrego-Varillas R, Ganzer L, Cerullo G and Manzoni C 2018 Ultraviolet transient absorption spectrometer with sub-20-fs time resolution *Appl. Sci.* **8** 989

[32] Ardini B, Manzoni C, Uboldi L and Richter F 2023 Raw Data of measurements at FERMI [Data set] *Zenodo* (https://doi.org/10.5281/zenodo.10059067)

[33] Iablonskyi D *et al* 2017 observation and control of laser-enabled Auger decay *Phys. Rev. Lett.* **119** 073203

[34] Koll L-M, Maikowski L, Drescher L, Witting T and Vrakking M J J 2022 Experimental control of quantum-mechanical entanglement in an attosecond pump-probe experiment *Phys. Rev. Lett.* **128** 043201

[35] Trinter F *et al* 2013 Vibrationally resolved decay width of interatomic coulombic decay in HeNe *Phys. Rev. Lett.* **111** 233004